nature materials

Letter

https://doi.org/10.1038/s41563-024-01894-0

Exceptional electronic transport and quantum oscillations in thin bismuth crystals grown inside van der Waals materials

Received: 29 November 2022

Accepted: 9 April 2024

Published online: 13 May 2024

Check for updates

Laisi Chen[1,9], Amy X. Wu[1,9], Naol Tulu[1], Joshua Wang[1], Adrian Juanson[2], Kenji Watanabe[3], Takashi Taniguchi[4], Michael T. Pettes[5], Marshall A. Campbell[1,5], Mingjie Xu[6], Chaitanya A. Gadre[1], Yinong Zhou[1], Hangman Chen[7], Penghui Cao[7], Luis A. Jauregui[1], Ruqian Wu[1], Xiaoqing Pan[1,6,8] & Javier D. Sanchez-Yamagishi[1]

Confining materials to two-dimensional forms changes the behaviour of the electrons and enables the creation of new devices. However, most materials are challenging to produce as uniform, thin crystals. Here we present a synthesis approach where thin crystals are grown in a nanoscale mould defined by atomically flat van der Waals (vdW) materials. By heating and compressing bismuth in a vdW mould made of hexagonal boron nitride, we grow ultraflat bismuth crystals less than 10 nm thick. Due to quantum confinement, the bismuth bulk states are gapped, isolating intrinsic Rashba surface states for transport studies. The vdW-moulded bismuth shows exceptional electronic transport, enabling the observation of Shubnikov–de Haas quantum oscillations originating from the (111) surface state Landau levels. By measuring the gate-dependent magnetoresistance, we observe multi-carrier quantum oscillations and Landau level splitting, with features originating from both the top and bottom surfaces. Our vdW mould growth technique establishes a platform for electronic studies and control of bismuth's Rashba surface states and topological boundary modes[1–3]. Beyond bismuth, the vdW-moulding approach provides a low-cost way to synthesize ultrathin crystals and directly integrate them into a vdW heterostructure.

Our understanding of two-dimensional (2D) electronic physics has been advanced by studying ultrathin vdW materials isolated by mechanical exfoliation[4]. However, this approach is generally inapplicable to other materials. The 2D growth of non-vdW materials is possible by molecular beam epitaxy (MBE) and other deposition techniques but often results in irregular surfaces or undesirable substrate interactions[5–8]. We consider an alternative 2D synthesis approach in which crystals are grown in the confined space between the layers of a vdW material. In confined growth, a mould defines the crystal geometry[9–13], but any surface roughness will be imprinted on the crystal and adversely affect electronic properties. Recently, it has been demonstrated that vdW materials can define atomically smooth channels of nanoscale thickness[14]. Such channels are difficult to achieve via other techniques and are attractive moulds for confined crystal growth.

Here we demonstrate confined growth of ultraflat bismuth between layers of hexagonal boron nitride (hBN), a vdW material. Bismuth has played a key role in the development of quantum electronic physics due to its low carrier density, small effective mass and ability to grow pristine bulk crystals[1,15]. Recently, the boundaries of bismuth have received attention due to its spin–momentum locking in 2D Rashba surface states and one-dimensional (1D) helical edge modes[1,2,16]. These boundary modes have been probed primarily by scanning tunnelling

A full list of affiliations appears at the end of the paper. e-mail: javier.sanchezyamagishi@uci.edu

https://doi.org/10.1038/s41563-024-01894-0

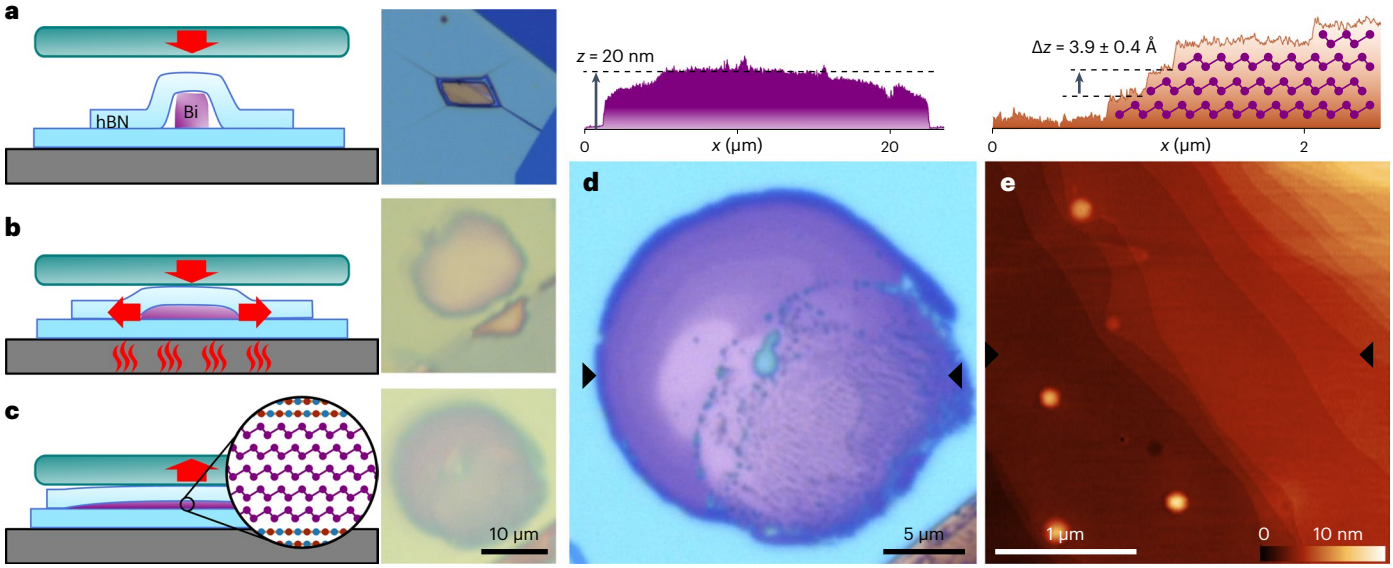

Fig. 1 | Growth of ultrathin bismuth crystals inside a vdW mould. a–c, Cross-sectional schematics of the vdW-mould process with corresponding optical images of the bismuth. **a**, Bismuth flake encapsulated in hBN on a bottom substrate of Si/SiO_2 before squeezing. **b**, Uniaxial compression (vertical red arrow) is applied to the stack by a rigid top substrate (glass or sapphire) while the stage is heated. When the bismuth reaches its melting point, it rapidly compresses and expands laterally. **c**, Bismuth is cooled below its melting point and then pressure is removed, resulting in an ultrathin bismuth crystal. The inset shows the atomic structure. **d**, Optical image of the encapsulated vdW-moulded bismuth (sample M30); black triangles indicate location of the AFM line trace (top) of the bismuth taken after removing the top hBN flake. This bismuth varies from 10 to 20 nm thick. **e**, AFM topography of the vdW-moulded bismuth after removing the top hBN, showing wide flat terraces. Black triangles show location of the line trace (top). The average step height is 3.9 ± 0.4 Å. The diagram inset in the shaded region shows the crystal structure.

microscopy (STM) and angle-resolved photoemission spectroscopy (ARPES), which have revealed diverse phenomena[2,5,17]. However, transport studies have been limited by disorder in the thin crystals where bulk conduction is gapped due to confinement. Via our vdW-moulding technique, we produce crystals that enable intrinsic transport studies of thin bismuth and its surface states.

Our process for growing crystals within a vdW mould is described in Fig. 1. First, a flake of bismuth is encapsulated in thin hBN layers using vdW transfer techniques[18] (Methods and Extended Data Fig. 1). Next, the bismuth–hBN stack is compressed between two substrates and then sequentially heated and cooled to melt and resolidify the bismuth (Fig. 1b). On melting, the bismuth rapidly spreads between the hBN layers and decreases in thickness due to the applied pressure. The squeezed form is retained when it is cooled into the solid phase and the pressure is released, resulting in a thin bismuth crystal encapsulated in hBN (Fig. 1c).

By squeezing the bismuth during the melting and solidification process, we reduced flakes that were 250–500 nm thick to ultrathin crystals ranging from 5 to 30 nm thick. Optically, the crystals exhibit large smooth areas with step-like contrast changes (Fig. 1d and Extended Data Fig. 2). These smooth areas emerge from a rougher material composed of both small voids in the crystal, likely due to trapped gas, and oxide that surrounded the original bismuth flake. After removing the top hBN layer, we characterize the bismuth surface by atomic force microscopy (AFM; Fig. 1e and Extended Data Fig. 3). The optically smooth regions correspond to flat terraces 0.5 to 5 μm wide separated by uniform steps. The average step height in Fig. 1e is 3.9 ± 0.4 Å, which matches the thickness of a buckled hexagonal layer of bismuth, also known as the (111) 'bilayer'[1].

To characterize the flatness of the vdW-moulded bismuth, we plot the distribution of height deviations across a wide terrace (Fig. 2a,b). Within the terrace of the vdW-moulded bismuth, the surface is ultraflat with an average root mean square deviation $\delta_{Bi-BN} = 0.11$ nm (Fig. 2b). By comparison, bismuth moulded by thermally grown SiO_2 exhibits a roughness of $\delta_{Bi-SiO_2} = 0.27$ nm. We ascribe this difference to the intrinsically flat structure of the vdW-layered hBN ($\delta_{BN} = 0.05$ nm) as compared to the amorphous SiO_2 ($\delta_{SiO_2} = 0.25$ nm). We have tested other mould substrates, such as graphite, sapphire and mica, and observed that the mould surface roughness is imprinted on the squeezed bismuth (Supplementary Section 2), with hBN producing the overall best results.

To determine the structure and crystallinity of the vdW-moulded bismuth, we performed transmission electron microscopy (TEM), electron backscatter diffraction (EBSD) and Raman spectroscopy (Methods and Supplementary Sections 3 and 4). All three measurements are consistent with the rhombohedral structure of bismuth. The TEM and EBSD diffraction measurements, performed on seven different samples, reveal that the bismuth is highly crystalline and oriented along the (111) axis, corresponding to buckled hexagonal layers stacked parallel to the substrate (Fig. 2e,f,h). The in-plane lattice constant measured from the real-space TEM image is 4.59 Å, which is within 1% of the bulk bismuth value 4.54 Å (ref. 1). Diffraction measurements show (111) domains many micrometres in width that are differentiated by relative in-plane rotations (Fig. 2h). Domain boundaries are also visible in AFM images (Supplementary Fig. 7). In some samples, the entire 20-μm-diameter flake is single crystal (Extended Data Fig. 4). The in-plane orientation of the bismuth shows no alignment with the encapsulating hBN. Additional discussion regarding domain structure can be found in Supplementary Sections 3 and 8.

By analysing 20 different growths, we find that vdW-moulded bismuth forms a dome shape with a typical thickness of 8 to 20 nm; terraces as thin as 5 nm can be observed near the crystal edge (Supplementary Fig. 2). The compression squeezes the bismuth until the top and bottom substrates elastically deform and contact around the bismuth–hBN stack, which we estimate to occur at 300 MPa pressure. Without compression, vdW moulding results in thicker bismuth crystals (thickness $t > 100$ nm). This behaviour is consistent with a continuum model, which predicts that thinner crystals are achievable by using more rigid substrates (Supplementary Section 5). Using sapphire top substrates instead of glass shows 40% thinner bismuth on average

https://doi.org/10.1038/s41563-024-01894-0

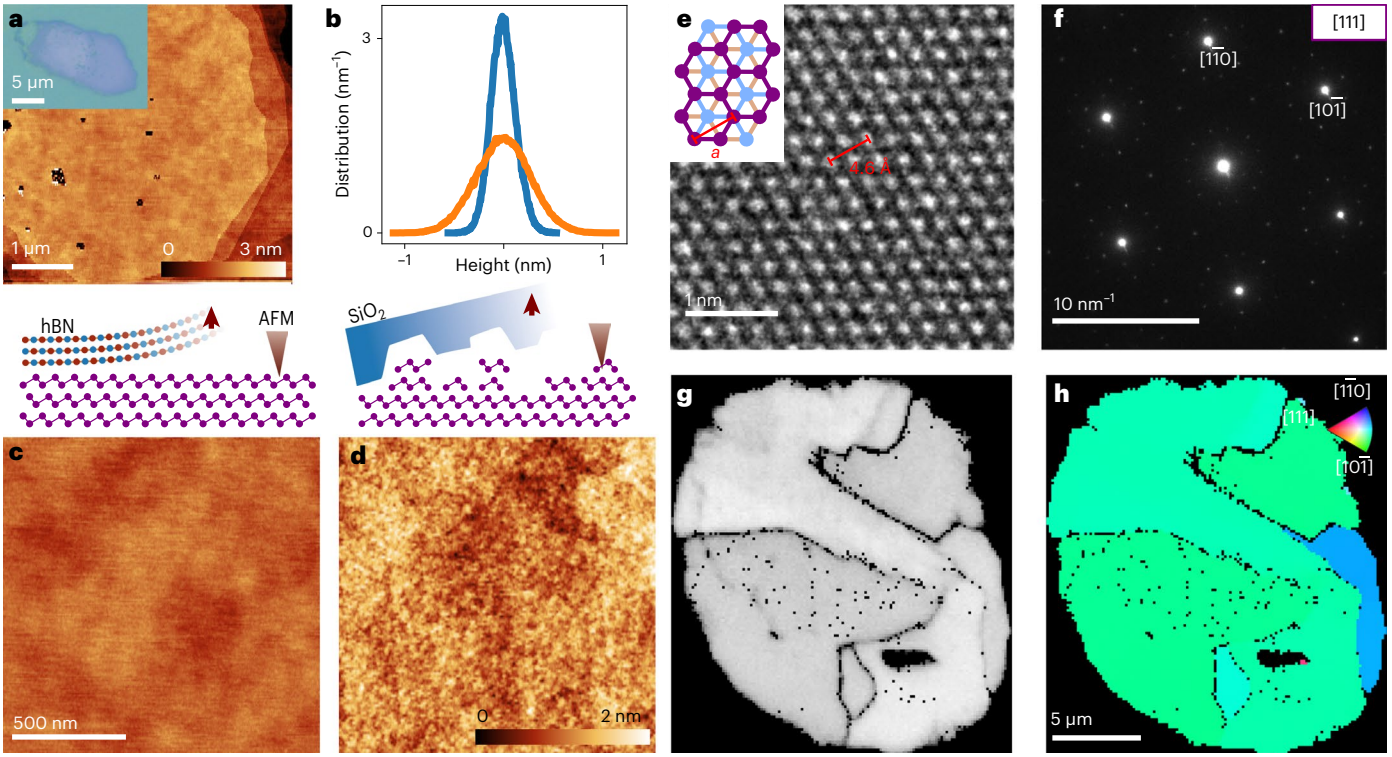

Fig. 2 | Flatness and crystallinity of vdW-moulded bismuth. a, AFM topography of vdW-moulded bismuth showing large flat terraces (sample M60). The inset shows an optical image of the sample. **b**, Height distribution of vdW-moulded bismuth (blue) and SiO_2-moulded bismuth (orange). **c**,**d**, AFM images of the surfaces of vdW-moulded bismuth (**c**) and SiO_2-moulded bismuth (**d**). Top substrates are removed before AFM. Scale bar is the same for both images, and the colour bar shows the height. The diagrams above depict the imprinting effect of the mould substrate on the bismuth. **e**, TEM real-space image of vdW-moulded bismuth. The inset shows the bismuth (111) lattice structure. **f**, TEM selected area electron diffraction (SAED) of vdW-moulded bismuth. **g**, EBSD band contrast of the vdW-moulded bismuth showing internal domain boundaries (dark lines). **h**, EBSD *Y*-axis inverse pole figure of (111)-orientated vdW-moulded bismuth showing domains with different in-plane rotations. Colours indicate the crystal orientation parallel to the in-plane *Y*-axis.

(Supplementary Fig. 1). The continuum model is also qualitatively consistent with atomistic simulations, which show the synthesis of even subnanometre-thick 2D crystals at high compression (Supplementary Fig. 10).

To electrically characterize the vdW-moulded bismuth, we fabricated devices in clean crystal regions composed of wide and flat terraces to minimize domain boundaries (Fig. 3, Methods and Extended Data Fig. 5). We measured both uniform-thickness devices etched from a single flat terrace and variable-thickness devices featuring many terrace steps. In all vdW-moulded bismuth devices, we observe metallic behaviour at low temperatures with a positive slope of resistance versus temperature, dR/dT (Fig. 3e and Extended Data Fig. 6). The slope decreases with rising temperature, unlike the linear T dependence observed in bulk bismuth, and is a signature of confinement effects in the vdW-moulded bismuth[15]. In thin devices, with thicknesses t = 8 nm and 13 nm, the metallic dependence persists to room temperature, but in thicker flakes, t = 45 nm to 106 nm, dR/dT can become zero or negative above ~50 K, indicating an activated dependence. This behaviour, measured in eight devices, is well modelled by parallel conduction through a metallic channel and a semiconducting bulk that is gapped due to vertical confinement[3,19,20] (Extended Data Fig. 6). The metallic channel is identified with the (111) Rashba surface states, which are known from ARPES and STM studies to have electron and hole pockets[3,21,22]. This is consistent with our observation of a positive non-saturating magnetoresistance in all devices up to 12 T (Fig. 3f and Extended Data Fig. 7), indicating nearly compensated electron-like and hole-like carriers.

The vdW-moulded bismuth exhibits exceptional transport properties compared to MBE-grown thin films. Previously, thin bismuth studies have been characterized by weak temperature dependences with little metallic contribution and small residual resistance ratios of 0.5 to 1.6 (refs. 19,23–25). By contrast, our vdW-moulded devices exhibit strong metallic dependencies, showing that surface-derived states can dominate the conduction at room temperature. This results in substantially larger residual resistance ratios, such as 12 and 5.4 for the flat 8 nm and 13 nm devices, respectively (additional devices in Extended Data Fig. 6). The substantially larger residual resistance ratio indicates reduced scattering times, which is also consistent with our observation of ×100 larger magnetoresistance signals than measured in MBE films (Fig. 3f).

At high fields, quantum oscillations in the magnetoresistance emerge in the vdW-moulded devices. The quantum oscillations are pervasive, occurring in 12 devices covering a wide range of thicknesses from 8 to 106 nm, with onset fields of 3 to 4 T (Fig. 3g and Extended Data Fig. 7). Even samples with non-uniform thicknesses and many terraces exhibit clean quantum oscillations (79 to 94 nm and 92 to 106 nm samples in Fig. 3g). Additional discussion on the possible role of terrace steps and domains on transport behaviours can be found in Supplementary Section 8. The dominant oscillations correspond to a Fermi surface area of 2×10^{12} to 3×10^{12} cm^{-2}, which are ×13–20 larger than that of bulk bismuth[26] and are consistent with STM and ARPES studies of the surface state[3,21,22]. Such Shubnikov–de Haas oscillations in the magnetoresistance were first observed in bulk bismuth[27].

The presence of quantum oscillations in vdW-moulded bismuth is striking, especially considering that the nanofabrication process exposes the bismuth to ambient air and polymers, which are avoided in MBE studies using in situ measurements[19,24]. A key difference is that MBE-grown bismuth has irregular surfaces with dense steps, typically

https://doi.org/10.1038/s41563-024-01894-0

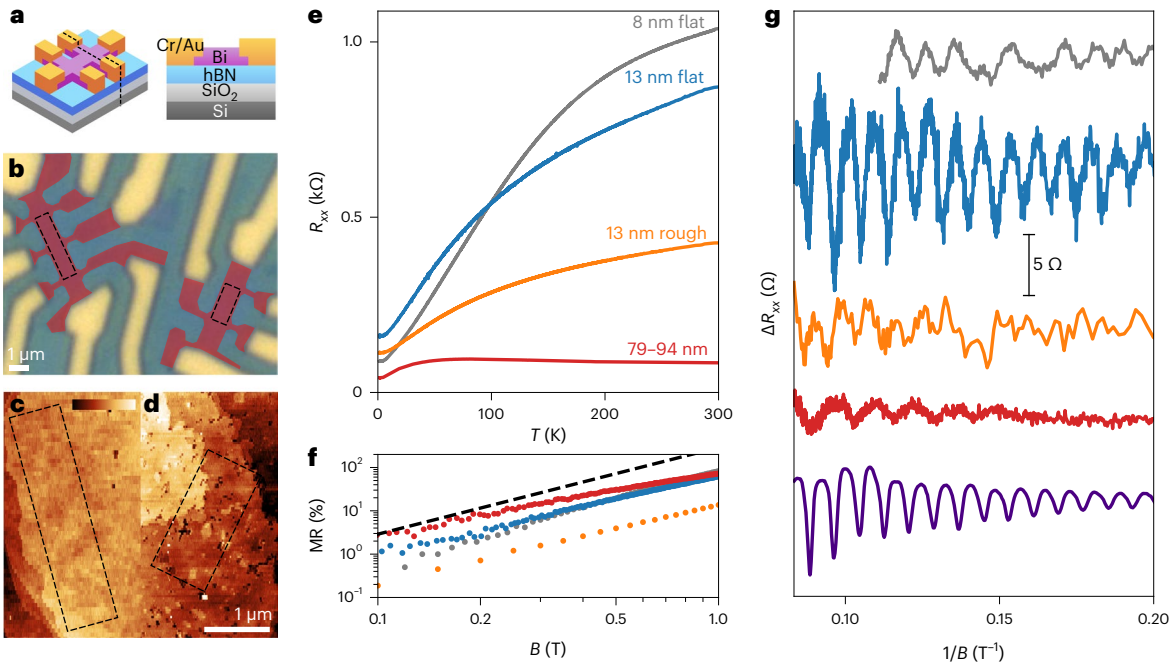

Fig. 3 | Electronic transport and quantum oscillations in vdW-moulded bismuth devices. a, Isometric and cross-sectional schematics of the devices. **b**, False colour optical image of the 13-nm-thick vdW-moulded bismuth devices; top hBN layer is removed. Bismuth is red, while gold electrodes are yellow. **c**,**d**, Surface topography of the 13-nm-thick bismuth devices; one is ultraflat (**c**; 0.8 μm × 3.6 μm) and the other is rough (**d**; 1.1 μm × 2.1 μm). Colour scale range is 0 to 2.5 nm and shows the height. Black dotted rectangles indicate the same regions on the bismuth devices in **b**. **e**, Longitudinal resistance (R_{xx}) as a function of temperature for different thickness devices. **f**, Logarithmic plot of magnetoresistance (MR) as a function of out-of-plane magnetic field ($T = 1.6$ K) for the same devices as in **e**. Black dashed line is quadratic dependence. **g**, Quantum oscillations in a plot of $\Delta R_{xx}(1/B)$, calculated by subtracting a smoothed background. Line colours correspond to the device labels in **e**. Additional data from a 92- to 106-nm-thick device is included (bottom-most purple line, scaled by ×0.05). Fermi surface areas from top to bottom are 2.75×10^{12}, 2.82×10^{12}, 2.99×10^{12}, 1.99×10^{12} and 2.60×10^{12} cm^{-2}.

20 to 100 nm apart[8,28], which can scatter electrons and provide parallel conduction[16,17]. By contrast, the vdW-moulded bismuth frequently exhibits 10 to 100 times wider terraces (Extended Data Fig. 3). The importance of surface flatness on transport properties is clear when we compare two devices from the same 13-nm-thick bismuth flake: one fabricated on an ultraflat terrace and the other on a rougher region (Fig. 3c,d). The rough device shows features qualitatively similar to the flatter device, but with reduced values for the residual resistance ratio, magnetoresistance and amplitude of quantum oscillations (Fig. 3e–g).

The quantum oscillations in the vdW-moulded bismuth disperse with back-gate voltage, resulting in clear Landau fan features (Fig. 4 and Extended Data Fig. 8). In the flat 13 nm device, two fans are observed with opposite slopes in the field-versus-gate space, indicating electron-like and hole-like carriers (Fig. 4c,e). At fields above 8 T, the hole fan changes to a different slope. At zero gate voltage, the $1/B$ frequencies of the oscillations, where B denotes the out-of-plane magnetic field, correspond to Fermi surface areas n of 2.77×10^{12} cm^{-2}, 0.73×10^{12} cm^{-2} and 1.94×10^{12} cm^{-2} for the electron and two hole pockets, respectively. Interestingly, each Fermi surface changes similarly over the 140 V gate voltage range with $\Delta n = 0.78$, 0.93 and 1.13×10^{12} cm^{-2}. By fitting Landau fans to the datasets, we observe that the highest gate voltage depletes the low-density hole pocket to Landau index $N_h = 2$. Such a large gate modulation is important, as the different Fermi surfaces are expected to carry different spin textures due to Rashba spin–orbit coupling[1].

Previous theoretical and ARPES studies of the bismuth (111) surface states have identified three types of Fermi surface: a gamma-point electron pocket, a six-fold degenerate hole pocket and a set of electron pockets near the M point (Fig. 4f)[3,20]. Landau level features have been observed only by STM and were ascribed to the gamma electron pocket and the oblong hole valleys[21,22]. The pocket sizes we observe are comparable to these previous studies, but it is surprising that all the pockets exhibit similar gate couplings despite large expected differences in their degeneracies. The origin of the change in the hole pocket size at fields above 8 T is also unknown (Fig. 4c).

Transport is differentiated by measuring contributions from the top and bottom surfaces, while STM and ARPES probe only the top. Generically, asymmetries between the surfaces are expected due to both the device structure and the applied electric fields. In the 13 nm device, we do not observe any splitting induced by the back-gate, suggesting that the surfaces are coupled due to proximity. Instead, we observe magnetic-field-induced splittings of the Landau levels at 11 T (Fig. 4c, yellow lines), which can arise from exchange-induced nematicity[22]. By contrast, in the 92–106 nm device (Fig. 4d), we observe clear gate-induced splitting of the electron-pocket Landau fan, resulting in two sets of oscillations with applied gate voltage, one strongly gate dependent and the other independent of gate. We ascribe these oscillations to the decoupled top and bottom surface states, where the bottom surface couples more strongly to the back-gate and screens the electric field from reaching the top surface. This demonstrates how the surfaces of thin bismuth crystals intrinsically support independently controllable 2D systems.

To summarize, we demonstrate a method to synthesize ultrathin and flat bismuth crystals within a nanoscale vdW mould. The confined bismuth exhibits gate-tunable quantum oscillations that originate from the (111) surface states. The bismuth surface bands are known to feature spin–momentum locking, which can be used to electrically generate spin polarizations[1,29–31]. Moreover, vdW-moulded bismuth can shed light on the transport behaviour of intrinsic helical edge modes that have been observed in STM[2].

Our mechanical modelling and atomistic simulations suggest that vdW moulding offers a route to 2D bismuthene, which is predicted to be

https://doi.org/10.1038/s41563-024-01894-0

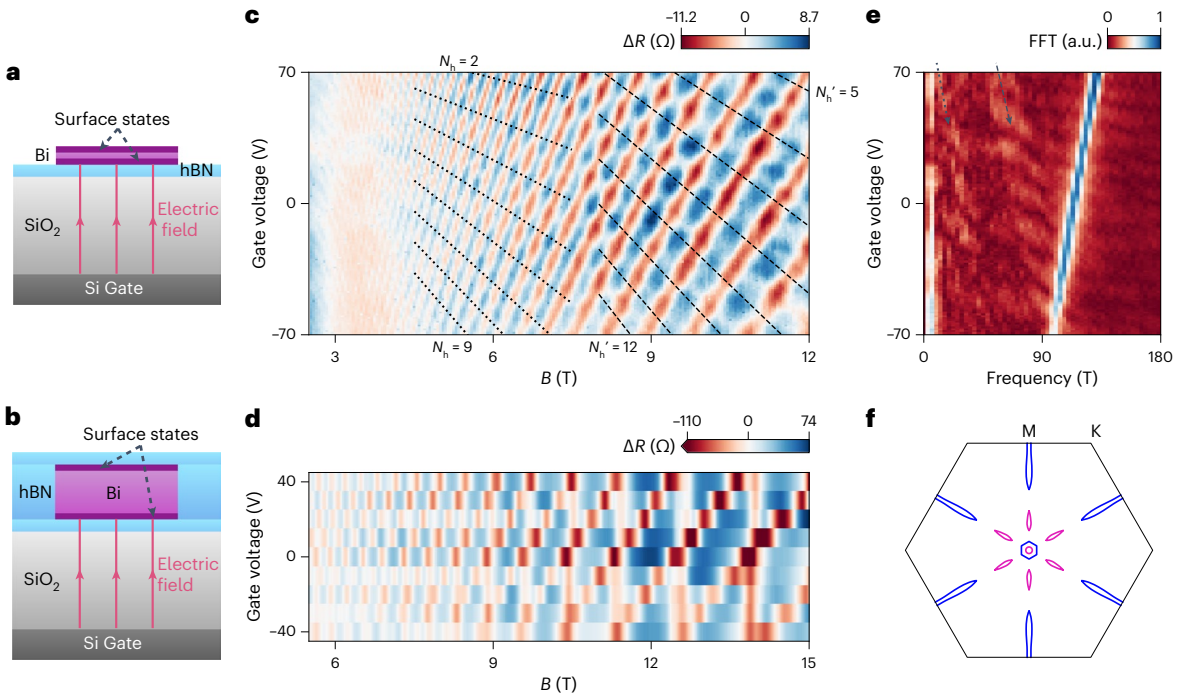

Fig. 4 | Gate-dependence and surface state coupling in thin and thick vdW-moulded bismuth. a, Cross-sectional schematics of a 13-nm-thick bismuth device showing similar gate capacitive coupling to the top and bottom surfaces. **b**, Cross-sectional schematics of a 92- to 106-nm-thick bismuth device showing larger capacitive coupling of the gate to the bottom surface. **c**,**d**, Quantum oscillations measured as a function of gate voltage and magnetic field for the flat 13 nm device (**c**; $T = 1.5$ K) and the 92–106 nm device (**d**; $T = 0.3$ K). The ΔR is calculated by subtracting a smooth background from magnetoresistance measurements. Landau fan fit is indicated by dashed lines based on **e**. Devices are the same as in Fig. 3. **e**, The fast Fourier transform (FFT) of the quantum oscillations shown in **c**, showing one electron-like oscillation (blue streak feature) and two sets of hole-like oscillations indicated by the dashed arrows (same as in **c**). **f**, Fermi surface diagram of bismuth (111) surface states based on density functional theory (DFT) calculations of 4.7-nm-thick bismuth (Extended Data Fig. 9). Blue, electron pockets; purple, hole pockets.

a large-gap 2D topological insulator[32,33]. Beyond bismuth, we anticipate that the vdW-mould technique will be applicable to other soft materials, enabling an approach combining ultrathin vdW and non-vdW materials.

Online content

Any methods, additional references, Nature Portfolio reporting summaries, source data, extended data, supplementary information, acknowledgements, peer review information; details of author contributions and competing interests; and statements of data and code availability are available at https://doi.org/10.1038/s41563-024-01894-0.

References

1. Hofmann, P. The surfaces of bismuth: structural and electronic properties. *Prog. Surf. Sci.* **81**, 191–245 (2006).
2. Schindler, F. et al. Higher-order topology in bismuth. *Nat. Phys.* **14**, 918–924 (2018).
3. Ito, S. et al. Surface-state coulomb repulsion accelerates a metal-insulator transition in topological semimetal nanofilms. *Sci. Adv.* **6**, eaaz5015 (2020).
4. Novoselov, K. S., Mishchenko, A., Carvalho, A. & Castro Neto, A. H. 2D materials and van der Waals heterostructures. *Science* **353**, aac9439 (2016).
5. Reis, F. et al. Bismuthene on a SiC substrate: a candidate for a high-temperature quantum spin Hall material. *Science* **357**, 287–290 (2017).
6. Vogt, P. et al. Silicene: compelling experimental evidence for graphenelike two-dimensional silicon. *Phys. Rev. Lett.* **108**, 155501 (2012).
7. Zhu, F. et al. Epitaxial growth of two-dimensional stanene. *Nat. Mater.* **14**, 1020–1025 (2015).
8. Hirayama, H. Nucleation and growth of ultrathin Bi films. *Adv. Phys. X* **6**, 1845975 (2021).
9. Li, R. et al. Atomic imprinting into metallic glasses. *Commun. Phys.* **1**, 75 (2018).
10. Li, L., Liu, J., Zeng, M. & Fu, L. Space-confined growth of metal halide perovskite crystal films. *Nano Res.* **14**, 1609–1624 (2021).
11. Liu, Z., Han, G., Sohn, S., Liu, N. & Schroers, J. Nanomolding of crystalline metals: the smaller the easier. *Phys. Rev. Lett.* **122**, 036101 (2019).
12. Hussain, N. et al. Ultrathin Bi nanosheets with superior photoluminescence. *Small* **13**, 1701349 (2017).
13. Li, C. et al. Synthesis of crystalline black phosphorus thin film on sapphire. *Adv. Mater.* **30**, 1703748 (2018).
14. Radha, B. et al. Molecular transport through capillaries made with atomic-scale precision. *Nature* **538**, 222–225 (2016).
15. Prakash, O., Kumar, A., Thamizhavel, A. & Ramakrishnan, S. Evidence for bulk superconductivity in pure bismuth single crystals at ambient pressure. *Science* **355**, 52–55 (2017).
16. Nayak, A. K. et al. Resolving the topological classification of bismuth with topological defects. *Sci. Adv.* **5**, eaax6996 (2019).
17. Drozdov, I. K. et al. One-dimensional topological edge states of bismuth bilayers. *Nat. Phys.* **10**, 664–669 (2014).
18. Purdie, D. G. et al. Cleaning interfaces in layered materials heterostructures. *Nat. Commun.* **9**, 5387 (2018).
19. Kröger, P. et al. Controlling conductivity by quantum well states in ultrathin Bi(111) films. *Phys. Rev. B* **97**, 045403 (2018).
20. König, C., Greer, J. C. & Fahy, S. Electronic properties of bismuth nanostructures. *Phys. Rev. B* **104**, 045432 (2021).
21. Du, H. et al. Surface Landau levels and spin states in bismuth (111) ultrathin films. *Nat. Commun.* **7**, 10814 (2016).

22. Feldman, B. E. et al. Observation of a nematic quantum Hall liquid on the surface of bismuth. *Science* **354**, 316–321 (2016).
23. Zhu, K., Wu, L., Gong, X., Xiao, S. & Jin, X. Quantum transport in the surface states of epitaxial Bi(111) thin films. *Phys. Rev. B* **94**, 121401 (2016).
24. Abdelbarey, D., Koch, J., Mamiyev, Z., Tegenkamp, C. & Pfnür, H. Thickness-dependent electronic transport through epitaxial nontrivial Bi quantum films. *Phys. Rev. B* **102**, 115409 (2020).
25. Aitani, M. et al. *In situ* magnetotransport measurements in ultrathin Bi films: evidence for surface-bulk coherent transport. *Phys. Rev. Lett.* **113**, 206802 (2014).
26. Dhillon, J. S. & Shoenberg, D. The de Haas-van Alphen effect III. Experiments at fields up to 32KG. *Philos. Trans. R. Soc. A Math. Phys. Eng. Sci.* **248**, 1–21 (1997).
27. Schubnikow, L. & De Haas, W. J. A new phenomenon in the change of resistance in a magnetic field of single crystals of bismuth. *Nature* **126**, 500–500 (1930).
28. Yaginuma, S. et al. Surface pre-melting and surface flattening of Bi nanofilms on Si(111)-7×7. *Surf. Sci.* **547**, L877–L881 (2003).
29. Jiang, Z., Soghomonian, V. & Heremans, J. J. Dynamic nuclear spin polarization induced by the Edelstein effect at Bi(111) surfaces. *Phys. Rev. Lett.* **125**, 106802 (2020).
30. Tian, J., Hong, S., Miotkowski, I., Datta, S. & Chen, Y. P. Observation of current-induced, long-lived persistent spin polarization in a topological insulator: a rechargeable spin battery. *Sci. Adv.* **3**, e1602531 (2017).
31. Bihlmayer, G., Noël, P., Vyalikh, D. V., Chulkov, E. V. & Manchon, A. Rashba-like physics in condensed matter. *Nat. Rev. Phys.* **4**, 642–659 (2022).
32. Murakami, S. Quantum spin Hall effect and enhanced magnetic response by spin-orbit coupling. *Phys. Rev. Lett.* **97**, 236805 (2006).
33. Liu, Z. et al. Stable nontrivial Z_2 topology in ultrathin Bi (111) films: a first-principles study. *Phys. Rev. Lett.* **107**, 136805 (2011).

[1]Department of Physics and Astronomy, University of California Irvine, Irvine, CA, USA. [2]Department of Physics and Astronomy, California State University Long Beach, Long Beach, CA, USA. [3]Research Center for Electronic and Optical Materials, National Institute for Materials Science, Tsukuba, Japan. [4]Research Center for Materials Nanoarchitectonics, National Institute for Materials Science, Tsukuba, Japan. [5]Center for Integrated Nanotechnologies (CINT), Materials Physics and Applications Division, Los Alamos National Laboratory, Los Alamos, NM, USA. [6]Irvine Materials Research Institute, University of California Irvine, Irvine, CA, USA. [7]Department of Mechanical and Aerospace Engineering, University of California Irvine, Irvine, CA, USA. [8]Department of Materials Science and Engineering, University of California Irvine, Irvine, CA, USA. [9]These authors contributed equally: Laisi Chen, Amy X. Wu. ✉e-mail: javier.sanchezyamagishi@uci.edu

Methods

Bismuth seed flake preparation

The starting point for vdW-mould growth is to prepare thin bismuth flakes that can be encapsulated[12]. First, a bismuth powder solution (Sigma-Aldrich, ~100 mesh, ≥99.99%, 140-µm-diameter bismuth in isopropyl alcohol or ethanol) is drop-casted on a Si/SiO_2 chip and covered by another Si/SiO_2 chip. The stacked chips are heated to 204 °C while being compressed in a hydraulic press to a pressure of ~6 MPa. The resulting hydraulically pressed bismuth flakes are typically around 300 nm to 400 nm thick and are used as the starting material in the hBN–bismuth–hBN stacks.

Process for encapsulating bismuth in hBN

To encapsulate bismuth between hBN, we follow the polycarbonate (PC)-based vdW dry-stacking technique[18] (Extended Data Fig. 1c–e). Some hBN flakes of 10 to 100 nm thickness are prepared by mechanically exfoliating bulk single crystals onto Si/SiO_2 chips. The hBN and bismuth flakes are then picked up by separate PC stamps (PC film mounted onto polydimethylsiloxane (PDMS) supports), and then sequentially transferred onto a chip to produce a hBN–bismuth–hBN stack. After each transfer step, the transferred PC film is dissolved in chloroform.

Microsqueezing set-up

The vdW moulding is performed in a homemade microsqueezing set-up (Extended Data Fig. 1a) that can apply pressure in a ~500 μm^2 region via a sapphire hemisphere. The set-up is designed to provide a simple way to bring two flat surfaces together while keeping their surfaces parallel and minimizing shear forces. The sapphire hemisphere is secured face-down on a glass slide mounted to an *XYZ* micromanipulator. A microscope enables in situ observation. The sample chip is mounted onto a glass slide with Kapton tape (2.5 mils), which also acts as a spacer to align the top substrate. A flexible top substrate made of a glass or sapphire coverslip (thickness, 0.19–0.23 mm) is placed on top of the spacer Kapton tape and secured with additional Kapton tape to prevent lateral motion. The top substrate is prevented from touching the chip by the Kapton tape spacers when no pressure is applied (Extended Data Fig. 1b).

The vdW-moulding process

The vdW-moulding process is carried out inside of a homemade glove bag with a constant flow of N_2 gas. Using the microsqueezing set-up, a sapphire hemisphere is aligned above the hBN–bismuth–hBN stack while the sample stage is heated to 150 °C. The sapphire hemisphere is then brought down into contact with the glass coverslip, bending it towards the hBN–bismuth–hBN stack. When the coverslip and the stack make contact, the bismuth is squeezed and expands. We increase the pressure until the top and bottom substrates fully deform and come into contact around the stack and the bismuth stops expanding. After the maximum pressure has been applied, we heat the sample to temperatures as high as 300 °C. Typically, we observe a sudden expansion of the bismuth at 260 °C, which we interpret as the melting point of the bismuth that is suppressed relative to the ambient 271 °C melting point by the high ~300 MPa pressures. The stage is cooled to room temperature before we lift the sapphire hemisphere and release the pressure from the stack.

Preparing thick vdW-moulded bismuth samples

To produce vdW-moulded bismuth that is greater than 45 nm in thickness, additional hBN spacer layers are stacked between the two hBN flakes. The thickness of the spacers determines the maximum thickness of the moulded bismuth. The spacer is added to the stack before the bismuth seed material is added. The rest of the process is the same as moulding bismuth between two hBN flakes.

Protecting from oxidation

Under ambient conditions, bismuth has a stable native oxide layer 1–2 nm thick[34]. At high temperatures close to the melting point, bismuth oxidizes rapidly in air. To reduce the ambient oxygen concentration we use a glove bag purged with N_2 gas, although this only slows the rate of oxidation[35]. More notable are the protective effects of hBN encapsulation[36], which prevents catastrophic oxidation of bismuth even without the use of a glove bag. Furthermore, we find that the pressure-induced deformation of the substrates around the bismuth–hBN stack is also effective in sealing the stack and reducing the rate of oxidation.

Removing the top hBN

To characterize the surfaces of our bismuth sample, we used a polyvinyl chloride (PVC) pillar stamp to remove the top hBN flake[37]. The PVC pillar is made by securing a PVC film (Riken Wrap from Riken Fabro) onto a micromoulded PDMS pillar that is 10 µm × 10 µm × 20 µm. Then, we approach the top hBN flake slowly with the PVC–PDMS pillar as we heat the stage to 55–70 °C (ref. 38). Once in contact, we slowly lift up the PVC–PDMS pillar stamp with piezo-motors, which peels the top hBN flake away from the bismuth.

TEM sample preparation

We transfer the vdW-moulded ultrathin bismuth onto a TEM grid (200 nm silicon nitride membrane TEM grid with 2.5 µm holes from Ted Pella) via the PVC transfer method explained previously[37]. Samples are measured in a JEOL-2100F TEM instrument with a Schottky-type field emission electron source with 80–200 kV acceleration voltage.

Density functional theory calculations

Our first-principles calculations are performed with the projector augmented-wave pseudopotentials[39,40] and the generalized gradient approximation of Perdew–Burke–Ernzerhof [41] using Vienna Ab initio Simulation Package[42] code. An energy cut-off of 450 eV and a 10 × 10 × 1 Monkhorst–Pack k-point grid is used[43]. The structure is optimized until the atomic forces are smaller than 0.01 eV $Å^{-1}$. The vacuum layer is larger than 19 Å to ensure decoupling between neighbouring nanostructures. For the vdW corrections, we used the DFT-D3 method[44,45].

Device fabrication details

The general device fabrication procedure is to isolate clean regions of vdW-moulded bismuth via etching and then attach electrodes to the crystal. Here, 'clean' refers to regions with wide and flat terraces where surface irregularities are minimized. This approach also minimizes internal domain walls, which appear as clear surface irregularities in the AFM images (Supplementary Fig. 7). The 8 nm and 13 nm devices are fabricated from vdW-moulded bismuth samples with the top hBN removed, and the main transport channel between the voltage tabs is from one terrace of uniform thickness. The fabrication procedure for the open-face devices is shown in Extended Data Fig. 5.

First, the top hBN flake is removed via the PVC method[37]. The uniform regions are identified by AFM and are etched out from the bismuth using a polymethyl methacrylate (PMMA) mask (Microchem, 950 A7, 1 µm thick) made by electron-beam lithography. The bismuth is then etched into the designed shape via Ar plasma etch (Plasma-Therm reactive ion etcher model 790) with the following parameters: 300 W power, 401 V d.c. bias voltage, 30 sccm Ar flow rate and 115 mtorr process pressure for 45 s. This is followed by an O_2 plasma etch to remove cross-linked PMMA, using 70 W power, 227 V d.c. bias voltage, an O_2 flow rate of 9.9 sccm and a process pressure of 70 mtorr for 10 s. The remaining PMMA etch mask is removed in acetone. Next, electrodes are defined by a PMMA mask written via electron-beam lithography (1-um-thick piece of 950 A5 PMMA) and developed by a 3:1 (volume ratio) mixture of isopropyl alcohol and water. Since the bismuth is exposed to air, a thin oxide layer forms at its surface and results in a large contact resistance. We remove the oxide layer by Ar ion milling (Intlevac Nanoquest 1) with a 400 V beam voltage, 30 mA beam current, 80 deg beam angle and 80 V acceleration voltage for 5 s at 10 °C, and immediately deposit 5 nm Cr and 15 nm Au on top without exposing

the bismuth to the atmosphere (Telemark 249). Finally, we evaporate additional metal onto the sample in a separate evaporator (Temescal CV-8; 5 nm Cr and 100 nm Au) and lift off the PMMA in acetone.

A similar fabrication process is also used to produce devices from encapsulated vdW-moulded bismuth samples without removing the top hBN. Note, when the top hBN is thin, we are still able to observe the bismuth terraces through the hBN by AFM (as shown in Extended Data Fig. 3). In the bismuth geometry-defining etch (Extended Data Fig. 5d), we perform an extra step of a SF_6 plasma etch to etch away the top hBN before etching the bismuth with the Ar plasma. The hBN etching parameters are 30 W power, 15 V d.c. bias voltage, a SF_6 flow rate of 10 sccm and a process pressure of 100 mtorr for 15 s. In the step where we define the electrodes (Extended Data Fig. 5g), a SF_6 plasma etch is used to remove the top hBN in the unmasked region before ion milling the bismuth oxide.

Additional transport data analysis

Extended Data Fig. 6 shows the temperature-dependent resistance measurements on various devices. We fit these data to a resistance model that consists of metallic conduction and activated conduction in parallel, where R_0 is the residual resistance, a is the metallic dependence prefactor, G_1 is the semiconducting dependence prefactor, E_g is the bulk gap and k_B is the Boltzmann constant[19].

$$R = \left[(R_0 + aT)^{-1} + G_1 \exp\left(-\frac{E_g}{2k_B T}\right)\right]^{-1}$$

The fitted curves are plotted as dashed lines on top of the sheet resistance in Extended Data Fig. 6a. The fitted parameter E_g is plotted as a function of device thickness in Extended Data Fig. 6b.

Data availability

All of the data that support the findings of this study are available via Zenodo at https://doi.org/10.5281/zenodo.10929346 (ref. 46).

Code availability

The code for the experimental data analysis is available from the corresponding author upon request.

References

34. Cronin, S. B. et al. Making electrical contacts to nanowires with a thick oxide coating. *Nanotechnology* **13**, 653 (2002).
35. Messalea, K. A. et al. Bi_2O_3 monolayers from elemental liquid bismuth. *Nanoscale* **10**, 15615–15623 (2018).
36. Cao, Y. et al. Quality heterostructures from two-dimensional crystals unstable in air by their assembly in inert atmosphere. *Nano Lett.* **15**, 4914–4921 (2015).
37. Wakafuji, Y. et al. 3D manipulation of 2D materials using microdome polymer. *Nano Lett.* **20**, 2486–2492 (2020).
38. Wakafuji, Y. et al. Evaluation of polyvinyl chloride adhesion to 2D crystal flakes. *npj 2D Mater. Appl.* **6**, 44 (2022).
39. Blöchl, P. E. Projector augmented-wave method. *Phys. Rev. B* **50**, 17953–17979 (1994).
40. Kresse, G. & Joubert, D. From ultrasoft pseudopotentials to the projector augmented-wave method. *Phys. Rev. B* **59**, 1758–1775 (1999).
41. Perdew, J. P., Burke, K. & Ernzerhof, M. Generalized gradient approximation made simple. *Phys. Rev. Lett.* **77**, 3865–3868 (1996).
42. Kresse, G. & Furthmüller, J. Efficient iterative schemes for *ab initio* total-energy calculations using a plane-wave basis set. *Phys. Rev. B* **54**, 11169–11186 (1996).
43. Methfessel, M. & Paxton, A. T. High-precision sampling for Brillouin-zone integration in metals. *Phys. Rev. B* **40**, 3616–3621 (1989).
44. Grimme, S., Antony, J., Ehrlich, S. & Krieg, H. A consistent and accurate *ab initio* parametrization of density functional dispersion correction (DFT-D) for the 94 elements H-Pu. *J. Chem. Phys.* **132**, 154104 (2010).
45. Grimme, S., Ehrlich, S. & Goerigk, L. Effect of the damping function in dispersion corrected density functional theory. *J. Comput. Chem.* **32**, 1456–1465 (2011).
46. Chen, L. et al. Exceptional electronic transport and quantum oscillations in thin bismuth crystals grown inside van der Waals materials. *Zenodo* https://doi.org/10.5281/zenodo.10929346 (2024).
47. Wu, Q., Zhang, S., Song, H.-F., Troyer, M. & Soluyanov, A. A. WannierTools: an open-source software package for novel topological materials. *Comput. Phys. Commun.* **224**, 405–416 (2018).
48. Mostofi, A. A. et al. An updated version of Wannier90: a tool for obtaining maximally-localised Wannier functions. *Comput. Phys. Commun.* **185**, 2309–2310 (2014).

Acknowledgements

The fabrication and measurement of ultrathin bismuth devices were primarily supported by the Air Force Office of Scientific Research under award numbers FA9550-21-1-0165 and FA9550-23-1-0454 (L.C. and A.X.W.). Materials characterization and technique development were supported by the National Science Foundation (NSF) Materials Research Science and Engineering Center (MRSEC) programme through the University of California (UC) Irvine Center for Complex and Active Materials Seed Program (DMR-2011967, A.X.W.). We acknowledge the use of facilities and instrumentation at the Integrated Nanosystems Research Facility (INRF) in the Samueli School of Engineering at UC Irvine and at the UC Irvine Materials Research Institute (IMRI), which is supported in part by the NSF MRSEC through the UC Irvine Center for Complex and Active Materials. Film deposition work was performed using instrumentation funded by Defense University Research Instrumentation Program (DURIP) award FA2386-14-1-3026. Raman spectroscopy was supported by the Laboratory Directed Research and Development programme of Los Alamos National Laboratory under project number 20210782ER (M.T.P. and M.A.C.). This work was performed, in part, at the Center for Integrated Nanotechnologies, an Office of Science User Facility operated for the US Department of Energy (DOE) Office of Science. Los Alamos National Laboratory, an affirmative action equal opportunity employer, is managed by Triad National Security, LLC, for the US Department of Energy's NNSA, under contract 89233218CNA000001. K.W. and T.T. acknowledge support from the Japan Society for the Promotion of Science (JSPS) KAKENHI (Grant Numbers 21H05233 and 23H02052) and World Premier International Research Center Initiative (WPI), MEXT, Japan. Another portion of this work was performed at the National High Magnetic Field Laboratory, which is supported by National Science Foundation Cooperative Agreement no. DMR-2128556 and the State of Florida. We thank I. Krivorotov and A. Khan for the assistance and use of their sputtering machine. We thank V. Fatemi, A. F. Young, M. Q. Arguilla and X. Yan for productive discussions and F. Guzman, M. Xu, J. Zheng and Q. Lin for technical assistance.

Author contributions

J.D.S.-Y. supervised the overall research. L.C., A.X.W., N.T., J.W. and A.J. prepared the samples. L.C. and A.X.W. performed the device measurements and analysed the experimental data. M.A.C. performed the Raman measurements. M.X. and A.X.W. performed and analysed the EBSD measurements. C.A.G. performed TEM measurements. Y.Z. performed the first-principles calculations. H.C. and P.C. developed the molecular dynamics simulations of squeezing models. K.W. and T.T. synthesized the hBN samples. L.A.J., J.D.S.-Y., X.P., M.T.P., R.W. and P.C. discussed the results and commented on the manuscript. L.C., A.X.W. and J.D.S.-Y. wrote the manuscript.

Competing interests
The authors declare no competing interests.

Additional information
Extended data is available for this paper at https://doi.org/10.1038/s41563-024-01894-0.

Supplementary information The online version contains supplementary material available at https://doi.org/10.1038/s41563-024-01894-0.

Correspondence and requests for materials should be addressed to Javier D. Sanchez-Yamagishi.

Peer review information *Nature Materials* thanks Joseph Falson and the other, anonymous, reviewer(s) for their contribution to the peer review of this work.

https://doi.org/10.1038/s41563-024-01894-0

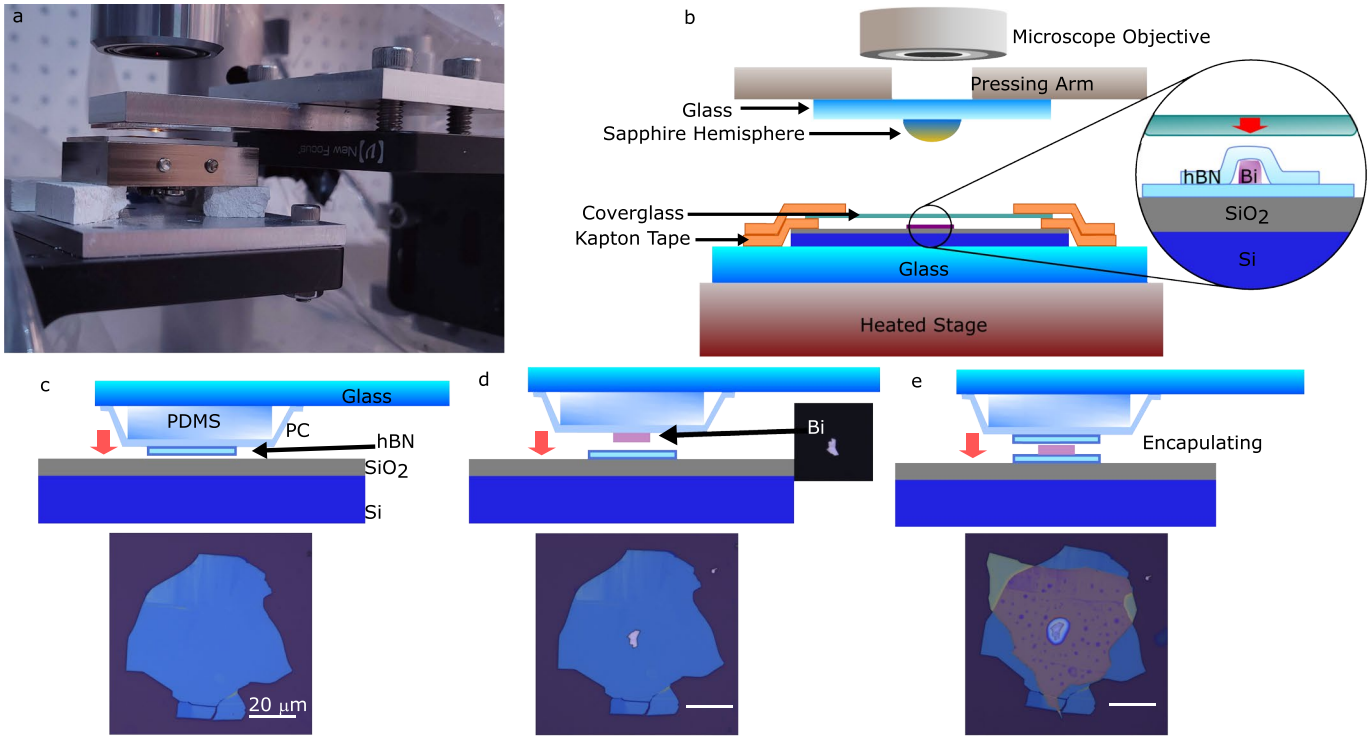

Extended Data Fig. 1 | Setup used for vdW-molding and process for preparing samples for vdW-molding. a, Photo of the microsqueezing setup. **b**, Diagram of the microsqueezing setup with inset of the sample stack. Setup is designed to keep the top and bottom substrates parallel during squeezing while minimizing shear forces. **c**-**e**, Diagram and optical sample image of each step to make a bismuth-hBN stack: **c**, transfer of bottom hBN flake onto substrate, **d**, transfer of starting bismuth flake on the bottom hBN, **e**, encapsulating bismuth with top hBN flake.

https://doi.org/10.1038/s41563-024-01894-0

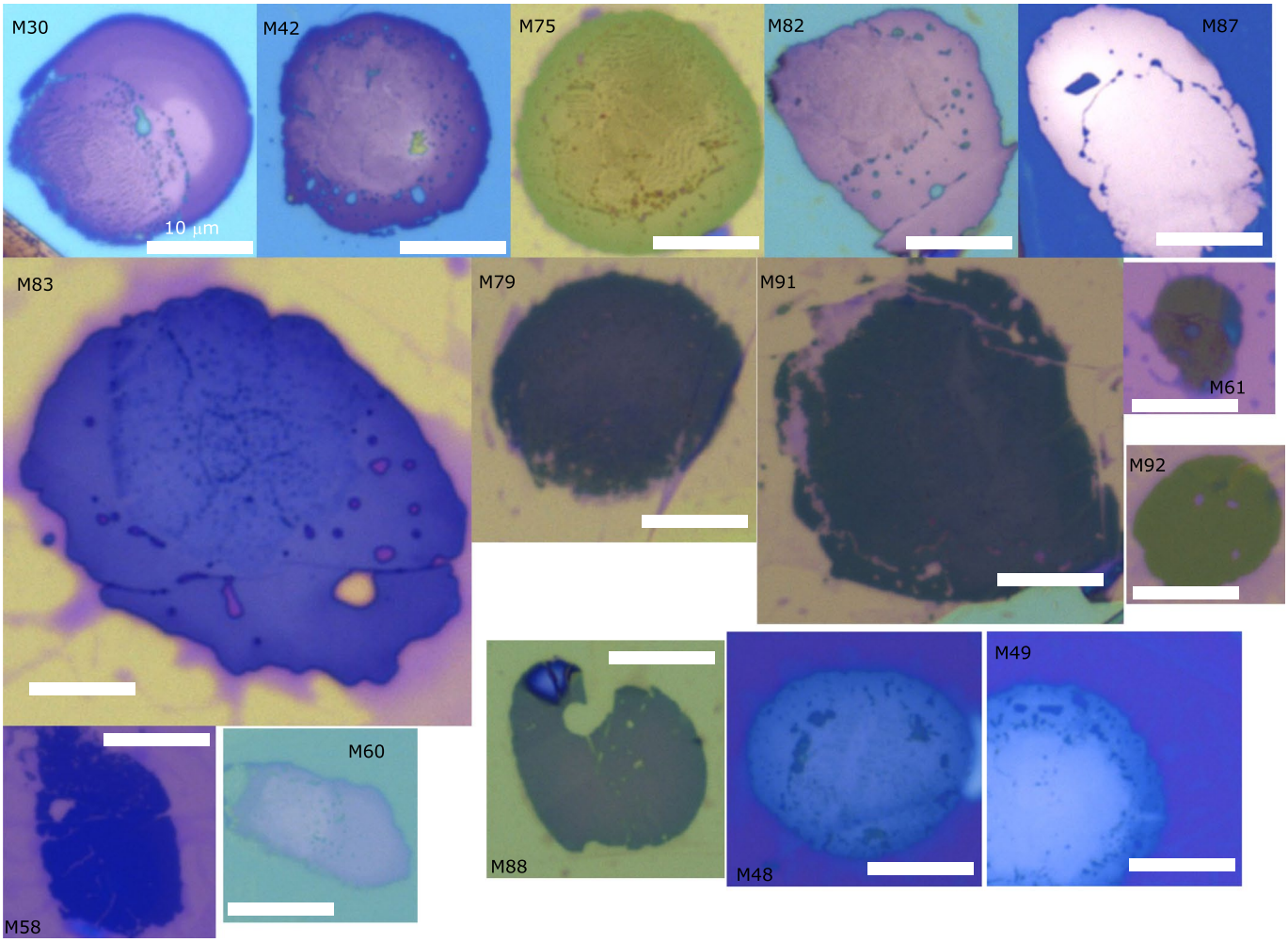

Extended Data Fig. 2 | Optical images of vdW-molded bismuth samples. For samples M60 and M87 the top hBN flakes have been removed. Scale bar is the same for all the images 10 μm.

https://doi.org/10.1038/s41563-024-01894-0

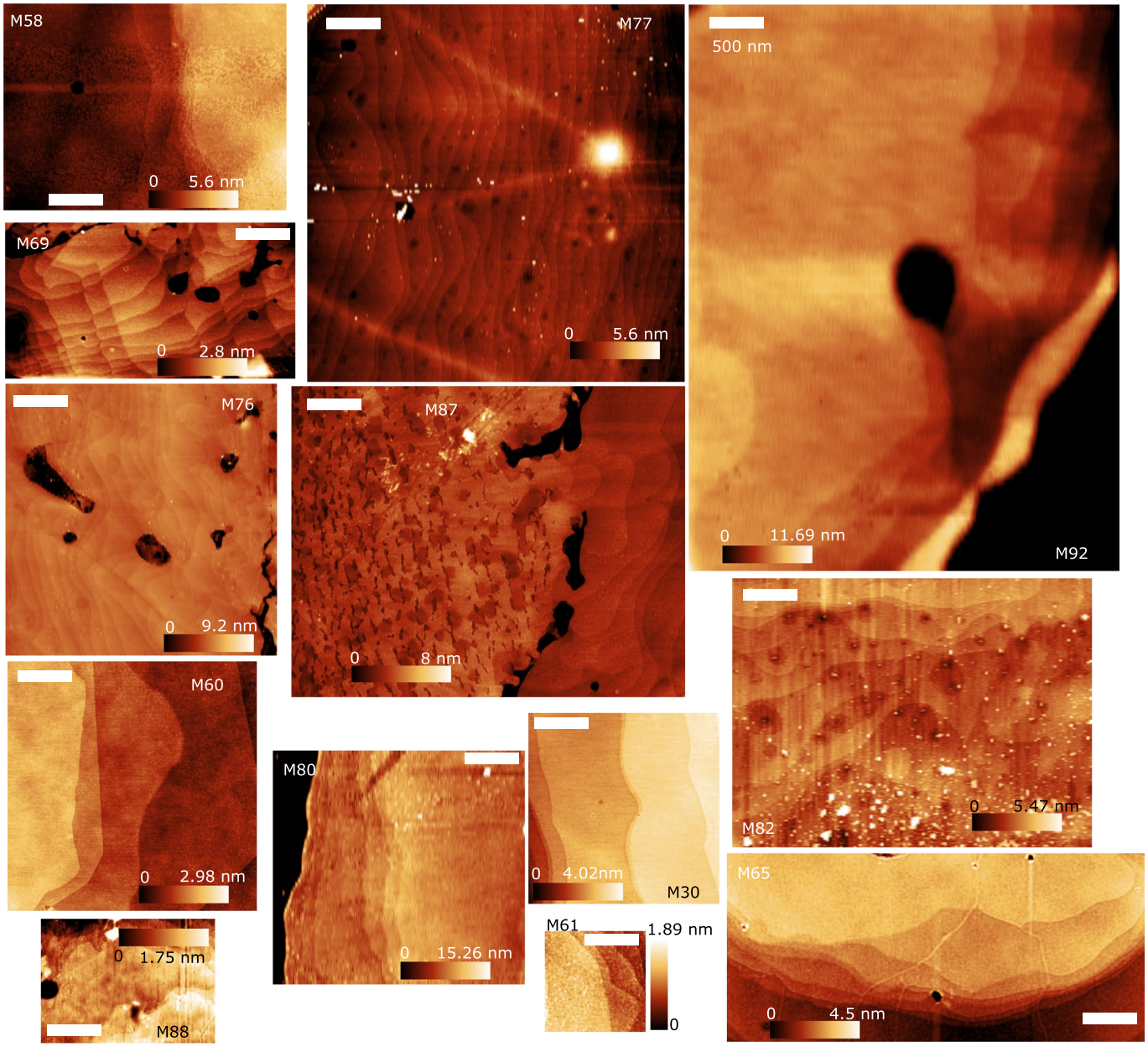

Extended Data Fig. 3 | AFM scans of the vdW-molded bismuth surfaces showing various flat terrace structures. All samples have the top hBN removed, except for M92. Clear layered terraces are visible in M92 through the thin hBN layer.

https://doi.org/10.1038/s41563-024-01894-0

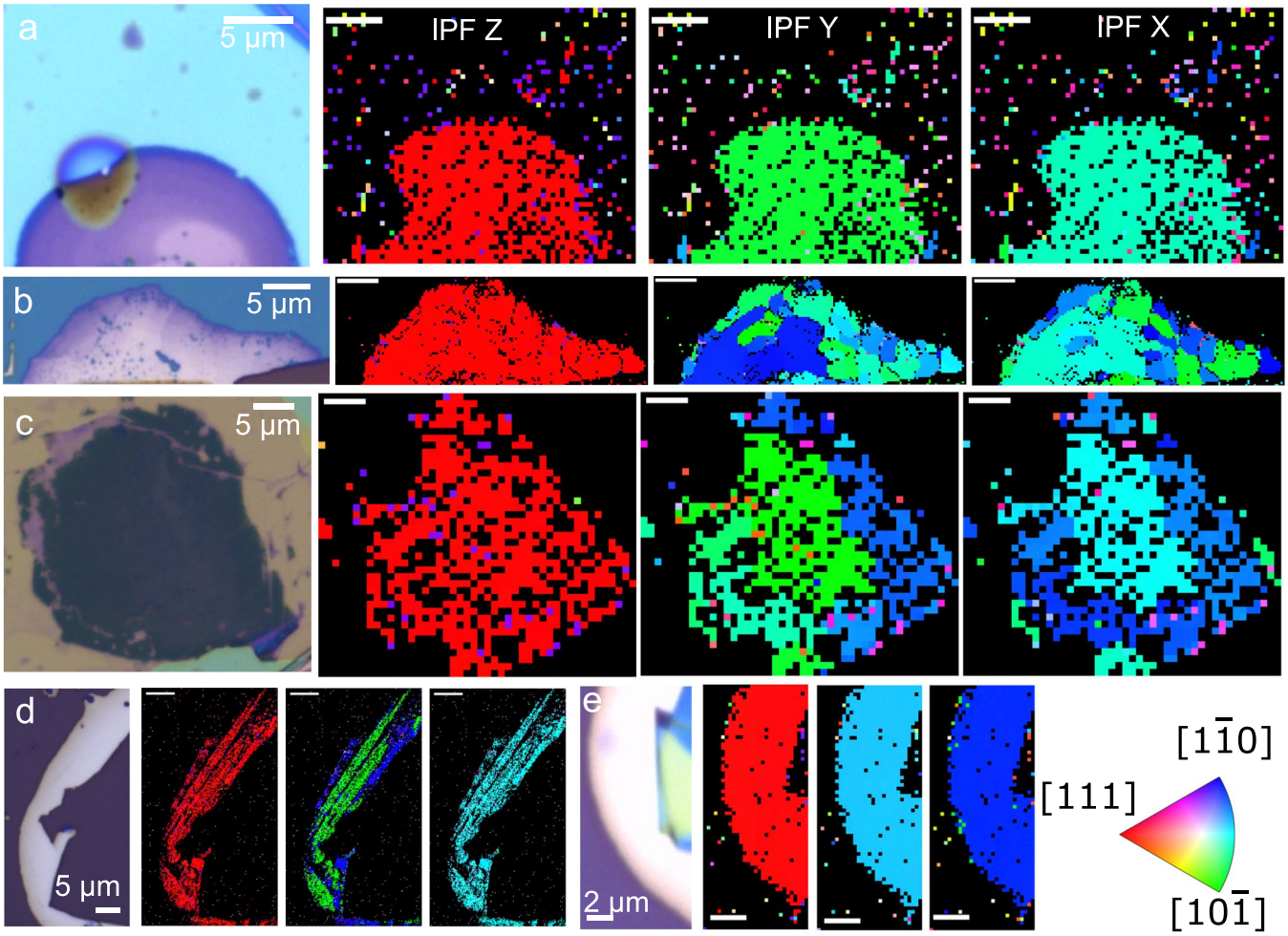

Extended Data Fig. 4 | Optical images and EBSD maps for additional samples. Optical image and X,Y,Z inverse pole figures are in respective order from left to right for each sample. **a&c**, vdW-molded bismuth encapsulated between hBN. **b**, vdW-molded bismuth without top hBN. **d-e**, SiO_2-molded bismuth on the edge of a hBN flake. Bismuth thickness for panels a-e are 21 nm, 23 nm, 17 nm, 20 nm – 61 nm, and 30 nm, respectively.

https://doi.org/10.1038/s41563-024-01894-0

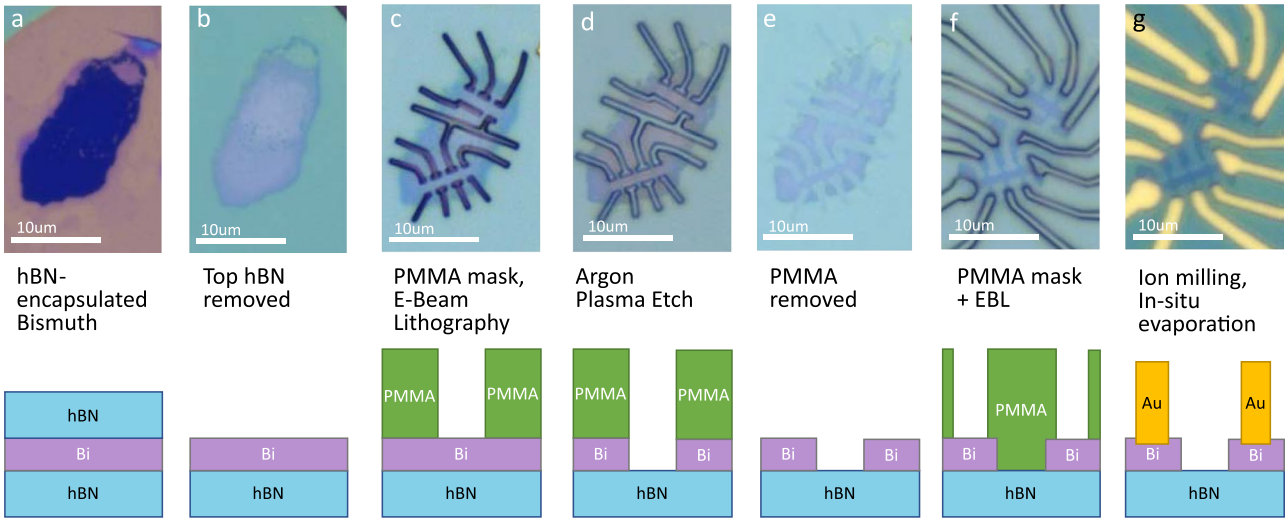

Extended Data Fig. 5 | Process for fabricating open-face devices from vdW-molded bismuth crystals. a-g, Optical image and cross-sectional schematics of the fabrication of the bismuth transport devices.

https://doi.org/10.1038/s41563-024-01894-0

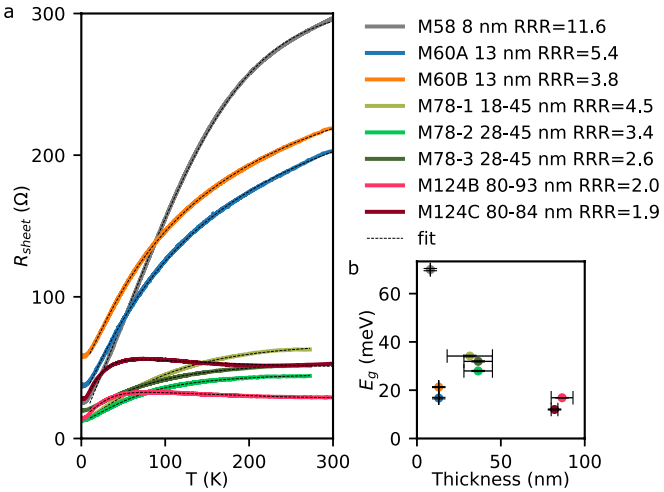

Extended Data Fig. 6 | Temperature-dependent transport measurements of various devices, plotted in designated colors. a, Sheet resistance as a function of temperature. **b**, Fitted bulk gap as a function of device thickness, averaged from the minimum and maximum thicknesses of each device. Vertical error bar denotes the standard deviation of the fitted bulk gap. Horizontal error bar denotes the range of the thickness of each device.

https://doi.org/10.1038/s41563-024-01894-0

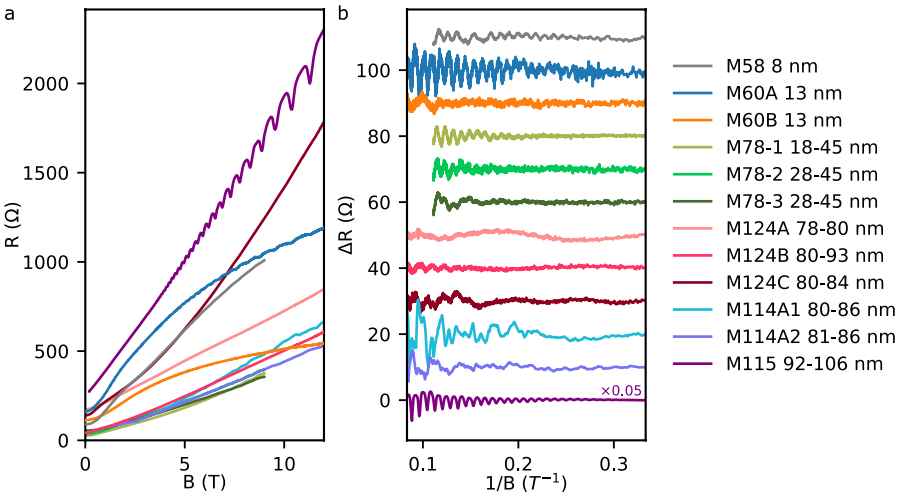

Extended Data Fig. 7 | Field-dependent transport measurements from various devices. a, Resistance as a function of magnetic field. **b**, Quantum oscillations in R(1/B) under 12 T, calculated by subtracting a smoothed background. Sample with a nonuniform thickness is labeled with a range.

https://doi.org/10.1038/s41563-024-01894-0

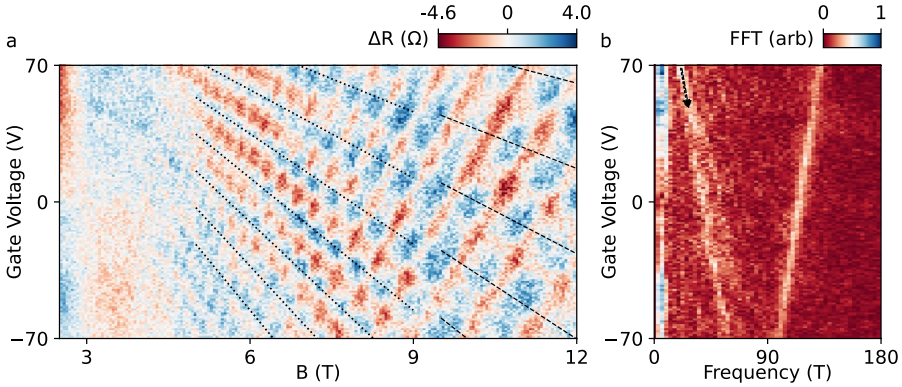

Extended Data Fig. 8 | Quantum oscillations measured in the rough 13 nm device. a, Quantum oscillations measured as a function of gate voltage and magnetic field for the rough 13 nm sample (1.1 µm x 2.1 µm) at 1.5 K. Same device as appears in Fig. 3. The amplitude of the quantum oscillation is much smaller in comparison to the flatter sample. **b**, FFT calculation of the quantum oscillation of the sample. Unlike the flat sample, we observe only one dominant hole oscillation.

https://doi.org/10.1038/s41563-024-01894-0

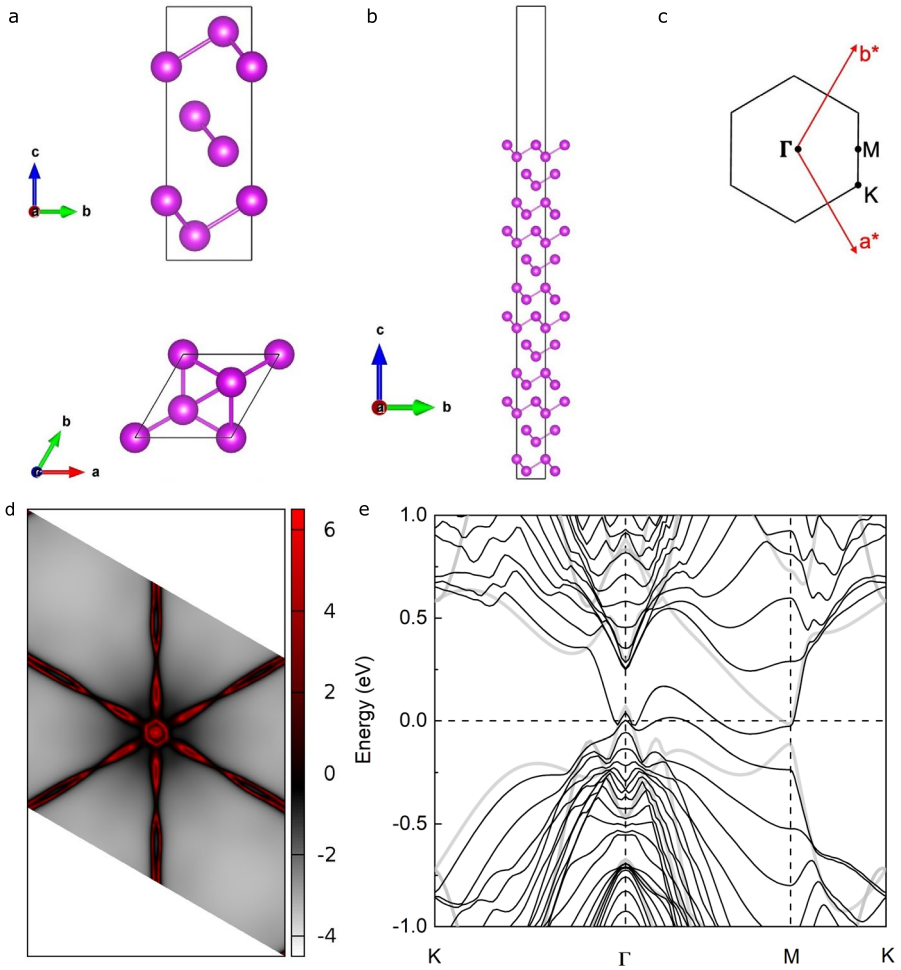

Extended Data Fig. 9 | DFT calculations of the lattice structure, Fermi surfaces, and band structure for 12-bilayer bismuth. a, Lattice structure of the bulk bismuth (111) for orientation aligned with the c-axis. The lattice constants are a = 4.57 Å, c = 11.75 Å and the Bi bond length is 3.10 Å. The intra-bilayer height is 1.63 Å and inter-bilayer spacing is 2.29 Å. **b**, Lattice structure of 12 bilayer bismuth with two (111) surfaces. After relaxation, the average of the intra bilayer height is 1.50 Å and inter bilayer spacing is 2.13 Å. **c**, The 2D first Brillouin zone of bismuth (111). **d**, Fermi surface at kz = 0, calculated using WannierTools[47] with a dense 201 × 201 × 1 k mesh, based on the tight-binding Hamiltonian obtained by employing maximally localized Wannier functions (MLWFs) method using WANNIER90[48] with initial projections to Bi-p orbitals. **e**, Band structure with Fermi surfaces at 0 eV. This plot is used as the basis of the Fermi surface schematic in Fig. 4f.